Quantifying the effect of anode surface roughness on diagnostic x-ray spectra using Monte Carlo simulation

A. Mehranian
Department of Medical Physics and Biomedical Engineering, Tehran University of Medical Sciences,
P.O. Box 14155-6447, Tehran, Iran and Research Center for Science and Technology in Medicine,
Tehran University of Medical Sciences, P.O. Box 14185-615, Tehran, Iran

M. R. Ay
Department of Medical Physics and Biomedical Engineering, Tehran University of Medical Sciences,
P.O. Box 14155-6447, Tehran, Iran; Research Center for Science and Technology in Medicine,
Tehran University of Medical Sciences, P.O. Box 14185-615, Tehran, Iran; and Research Institute for
Nuclear Medicine, Tehran University of Medical Sciences, P.O. Box 14155-6447, Tehran, Iran

N. Riyahi Alam
Department of Medical Physics and Biomedical Engineering, Tehran University of Medical Sciences,
P.O. Box 14155-6447, Tehran, Iran

H. Zaidi[a]
Division of Nuclear Medicine, Geneva University Hospital, CH-1211 Geneva, Switzerland
and Geneva Neuroscience Center, Geneva University, CH-1205 Geneva, Switzerland

Purpose: The accurate prediction of x-ray spectra under typical conditions encountered in clinical x-ray examination procedures and the assessment of factors influencing them has been a long-standing goal of the diagnostic radiology and medical physics communities. In this work, the influence of anode surface roughness on diagnostic x-ray spectra is evaluated using MCNP4C-based Monte Carlo simulations.

Methods: An image-based modeling method was used to create realistic models from surface-cracked anodes. An in-house computer program was written to model the geometric pattern of cracks and irregularities from digital images of focal track surface in order to define the modeled anodes into MCNP input file. To consider average roughness and mean crack depth into the models, the surface of anodes was characterized by scanning electron microscopy and surface profilometry. It was found that the average roughness (R_a) in the most aged tube studied is about 50 μm. The correctness of MCNP4C in simulating diagnostic x-ray spectra was thoroughly verified by calling its Gaussian energy broadening card and comparing the simulated spectra with experimentally measured ones. The assessment of anode roughness involved the comparison of simulated spectra in deteriorated anodes with those simulated in perfectly plain anodes considered as reference. From these comparisons, the variations in output intensity, half value layer (HVL), heel effect, and patient dose were studied.

Results: An intensity loss of 4.5% and 16.8% was predicted for anodes aged by 5 and 50 μm deep cracks (50 kVp, 6° target angle, and 2.5 mm Al total filtration). The variations in HVL were not significant as the spectra were not hardened by more than 2.5%; however, the trend for this variation was to increase with roughness. By deploying several point detector tallies along the anode-cathode direction and averaging exposure over them, it was found that for a 6° anode, roughened by 50 μm deep cracks, the reduction in exposure is 14.9% and 13.1% for 70 and 120 kVp tube voltages, respectively. For the evaluation of patient dose, entrance skin radiation dose was calculated for typical chest x-ray examinations. It was shown that as anode roughness increases, patient entrance skin dose decreases averagely by a factor of 15%.

Conclusions: It was concluded that the anode surface roughness can have a non-negligible effect on output spectra in aged x-ray imaging tubes and its impact should be carefully considered in diagnostic x-ray imaging modalities. © *2010 American Association of Physicists in Medicine.*
[DOI: 10.1118/1.3284212]

I. INTRODUCTION

Detailed and accurate knowledge of diagnostic x-ray spectra and factors influencing them is of great importance in many diagnostic x-ray imaging applications,[1,2] especially in the evaluation of patient dose, assessment of image quality,[3–6] and performance characterization of imaging systems,[7,8] which are particularly applied to novel technologies such as the recently developed flat-panel imagers.[9,10] During the last few decades, extensive efforts have been directed toward gaining this knowledge through experimental measurements and analytic computational predictions. Although experimental measurements using high resolution spectrometers have been widely adopted,[11–13] their use under clinical conditions has many limitations and calls for stringent procedures usually involving the application of special energy correction techniques. Hence, as far back as the early 1920s, there has been an increasing interest in the development of computational models for prediction of x-ray spectra under conditions typically encountered in clinical setting. The main advantage of computer modeling is that it allows separating out effects which cannot be isolated and studied in physical experiments.

Depending on the underlying prediction method used, computational models are divided into two main categories: Analytical and Monte Carlo models.[14] The analytical models can be further divided into empirical and semiempirical. Empirical models are based on the reconstruction of x-ray spectra from experimentally measured transmission data. They mostly rely on Laplace transform pairs,[15] numerical iterative techniques[16] and interpolating polynomial fit methods.[17,18] Semiempirical models, which were first established by Kramers,[19] are based on quantum mechanics theory of bremsstrahlung x-ray production[20] in which the differential cross section is formulated by empirically parameterized differential equations. After Kramers' work in 1923, these models underwent numerous improvements that made them capable to embrace as many radiation physics as they could afford. In 1976, Soole[21] modified the model of Kramers to include target attenuation. Birch and Marshal[22] adjusted empirically some parameters in the latter model and further improved it such that it could consider characteristic x rays and make fairly accurate predictions. Afterward, this model was improved by other researchers by including backscatter electrons,[20] depth-dependent production of x-ray photons,[23] and the spectra in molybdenum targets.[24] Although, in principle, x-ray spectra can be computed from analytical models, Monte Carlo (MC) simulation has proven to be the most accurate method for the prediction of electron-induced spectra[25] as a result of the rigorous modeling of stochastic processes through random sampling of radiation transport mechanisms.[26] MC simulations are applicable to experiments that cannot ever be performed in the laboratory, for example, separating out the signal contribution in a radiography system from primary and secondary radiation.[27] By means of MC models, it is possible to gain detailed knowledge of x-ray spectra from their outset site in the x-ray tube, through the patient and imaging chain, to the absorption spectrum at the image receptor.

The characteristics of an output x-ray spectrum are governed primarily by tube voltage, added filtration, target material, anode angle and configuration, and conditions of the anode surface. From their emission point in the anode block to exit window, x-ray photons experience a tube-specific attenuation pertaining to several absorbing materials, which is collectively referred to as inherent filtration.[28] By attenuating low-energy x rays to a greater extent than those with high energy, the inherent filtration contributes effectively to the output x-ray yield. An initial, sometimes significant, inherent filtration takes place within the anode material in which the x rays encounter some attenuation depending on tube voltage, anode angle, and the conditions of the focal path surface. As bombarding electrons are slowed down by numerous collisions with the anode material, almost more than 99% of their energy is degraded to heat within the target.[29] Immediately upon being struck by these electrons, the surface of focal spot undergoes a thermal load that rises its temperature to approximately 2500 °C and over time leads to its roughening and formation of cracks.[30] As a result, the penetration of striking electrons and production depth of the associated x rays become deeper and the inherent filtration is, therefore, increased via this added self-filtration. The anode roughening and its end effect on x-ray spectra have been studied by several authors. Nagel[31] treated experimentally the subject matter and reported that the half value layer (HVL) of emitted spectra after six months of tube operation increased up to 0.5 mm Al, whereas the tube output is reduced by more than 10% at 80 kVp and 2.5 mm Al filtration. In another study, a variation of about 0.2 mm Al in HVL for an anode roughness of 5 μm at 70 kVp and 2.5 mm Al filtration was determined semiempirically.[32] The same group reported that anodes with a surface roughness of about 1.4–3.8 μm correspond to additional filtration by tungsten with a thickness of 2.12–8.21 μm.[33] Other investigators presented detailed measurements of anode surface profiles of 19 diagnostic x-ray tubes and predicted empirically an intensity loss of 4% for rough anodes with 8 μm deep cracks.[34]

Although Monte Carlo simulation has experienced considerable growth both in terms of number of articles and diversity of studies,[35] to the best of the authors' knowledge, this is the first attempt to address the issue of anode roughening as a factor influencing x-ray spectra through MC modeling. The limited applicability of analytical models for treating anode roughness on one hand and our previous experience with MCNP[36,37] on the other hand motivated us to carry out this work through MC-based simulation. In this work, the influence of anode roughening on x-ray spectra was evaluated qualitatively and quantitatively for different rough anodes at various anode angles and tube voltages. In addition, the variations in output intensity, HVL, anode heel effect, and patient dose were comprehensively assessed.

II. MATERIALS AND METHODS
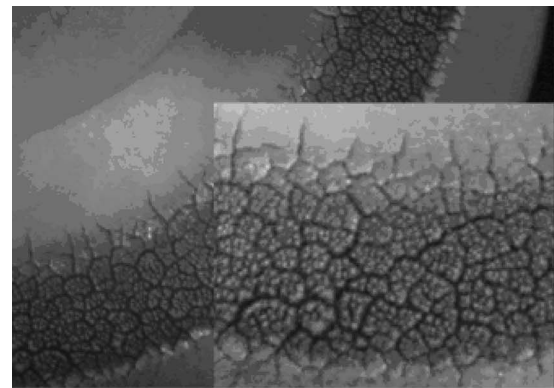
II.A. The MCNP Monte Carlo code

The MCNP code, a well-established general-purpose code for MC simulation of radiation transport, developed and maintained at Los Alamos National Laboratory (New Mexico, 87544),[38] was used to perform MC calculations. Although the MCNP code was originally designed and utilized for neutron and photon transport problems, it has incorporated an enhanced electron physics transport and now has become one of the most widely used MC codes by the radiological and medical physics communities. The rising desire in employing this code returns to its detailed physics treatment, extremely powerful geometry package, various scoring capabilities, and extensive internal error-checking routines. For photons, it takes into account photoelectric absorption, pair production, incoherent (Compton) and coherent (Rayleigh) scattering processes, and the possibility of fluorescent emission after photoelectric absorption. A continuous slowing down energy loss model is used for electron transport by considering angular deflection through multiple Coulomb scattering, collisional energy loss with optional straggling, and the production of secondary particles including K x rays and knock-on and Auger electrons. Over the years, the code has undergone considerable renovations and its capabilities enhanced with new features. In this work, we used the MCNP4C version run on Pentium IV dual core PC with 2.6 GHz CPU and 2 GB RAM.
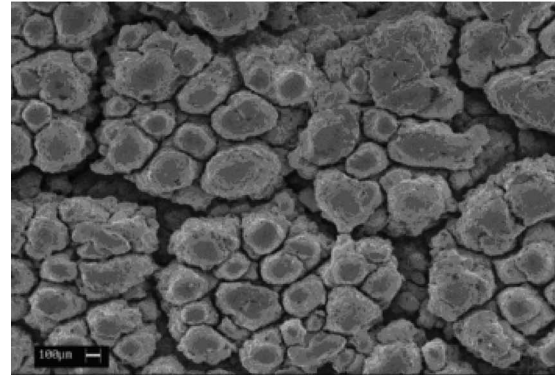
II.B. Anode surface modeling

To obtain realistic results, the geometry of the anode blocks and their cracked surfaces had to be described into MCNP's environment in as much detail as technical constraints allow. For this purpose, an image-based modeling method was followed which made it possible to consider the spatial pattern of cracks in accordance with the anodes' surface. By following this approach (see detailed description below), anode models were defined into MCNP code using digital images of the focal path (at least three times larger in width than a typical focal spot) and the information incorporated into their matrices.
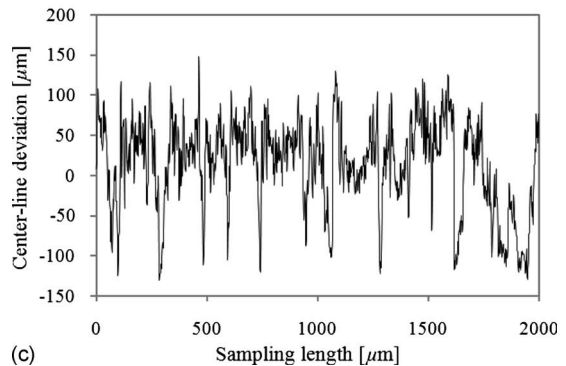
II.B.1. Anode surface data

Several x-ray tubes that have been heavily overworked were chosen and their anode surfaces analyzed after cutting out small pieces of their focal path using precise wire cut machine. For our modeling, several digital images were taken from focal paths in several spots using a digital camera. As shown in Fig. 1(a), which pertains to the most aged tube studied, the focal surface is so eroded that its cracked and grainy appearance can be observed with the naked eye. The branching pattern of cracks and their invasion into off-focus regions is well depicted in the foreground of this picture. As can be seen, there are regions that have been surrounded by coarser cracks and broken up by finer ones. Hereafter, we refer to the former as parent cracks and the latter as daughter cracks. To characterize the surfaces in

FIG. 1. (a) A digital image taken from the most aged anode disk studied in this work (background) and a close-up from its focal path surface (foreground). (b) A SEM image from the central part of the focal path shown in (a) with 30 times magnification. (c) Surface profile from the focal path shown in (a) measured in radial direction which shows deviation from center line versus sampling length.

terms of surface profiles, anode samples were studied by a profilometer (Taylor Hobson Surtronic, Leicester, U.K.). The surface morphology was further assessed by scanning the most deteriorated focal path using a LEO 440 scanning electron microscope (SEM). Figure 1(b) shows a cross sectional SEM image of that focal path with a magnification of 30. Being under the impact of energetic electrons and the heat power raised from their collisions has led to this focal path, which had been once perfectly plain, to be so much smashed and fractured. SEM measurements revealed valuable details about the grains and cracks. Assuming that grains are circu-

lar in their outer limits, the average radius of circles best fitting them was determined to be about 80 ± 20 μm. Also by supposing that cracks are rectangular valleys, it was determined that parents and daughters can have a width of approximately up to 100 and 20 μm, respectively. The roughness profile obtained from the profilometer shown in Fig. 1(c) indicated that the deepest cracks for the most deteriorated anode could deepen to approximately 130 μm into anode surface, whereas the mean average of surface roughness (R_a) could go up to around 50 μm.

II.B.2. MCNP geometry description

MCNP uses a flexible scheme for geometry definition in which geometrical volumes, known as cells, are primarily defined by Boolean combination of signed half spaces, which are delimited by first, second, and fourth degree surfaces in a three-dimensional Cartesian coordinate system. In this geometry definition, surfaces are in turn designated by special characters followed by appropriate coefficients needed to meet the surface equation. As an example, a cube can be defined by Boolean intersection of six planes (first degree surfaces).

II.B.3. Surface models

Our modeling process is based on the concept that a cracked and rough surface can be modeled into MCNP's environment by arranging a two-dimensional array of many height-differed cubes on a common base plane, in such a way that each cube's height and location are determined from a preprocessed image matrix. In this approach, one can imagine as if cubes have been overlaid on the image matrix and each one has received its height from the gray value of its underlying pixel. In other words, each pixel of focal path's processed image can represent one cubic cell in the anode surface model. To implement this concept into an MCNP input file, a computer program was written in MAT-LAB (MathWorks Inc., Natick, MA) to define the cubic cells in the same number of pixels as does the image possess. It then raises the height of each cube to its predetermined value. Given that the centimeter is the unit of length in MCNP, the image matrices were numerically processed such that the depth of cracks is incorporated into pixel values in agreement with the measured average depths. Due to the large number of cells and surfaces, a trade-off between the level of models' complexity and MCNP's efficiency was admitted. As shown in Fig. 2(b), the roughness of regions bounded by parent cracks was therefore ignored during the processing of focal paths' image. In addition, the image matrix sizes were shrunk by nearest-neighbor interpolation. Finally, for defining surface models in an optimized way without sacrificing their details, the written code was further developed in such a way that neighboring cells having the same height are merged into a larger cell. As illustrated in Fig. 2(c), this code combines cells if they share a common boundary, are bounded by the same surfaces in the directions perpendicular to the common boundary, and have the same height. The cell combination algorithm first searches for candidate cells with common boundaries in the direction of columns and then rows of the image. The CAD visualization was made from produced MCNP input file using MCAM, an integrated interface program between CAD systems and Monte Carlo simulation codes.[39] The width and length of each cube were scaled so that the dimensions of the model matched closely those of the actual selected focal path. The anode angle is considered in geometry definition by rotating all anode surface planes around an axis to the value of the anode angle.
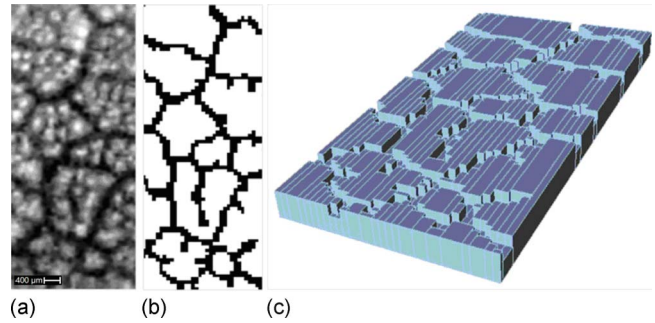

FIG. 2. Illustration of the modeling process of a surface-cracked anode in the 3D coordinate system of MCNP. The digital image of the focal region (a) is processed such that the pattern and mean depth of main cracks is rendered into image matrix (according to surface profilometries, each dark pixel is assigned a depth number) (b). (c) An optimized anode model based on the image shown in (a) visualized by MCAM (Ref. 39).

II.C. Simulation and detection of x-ray spectra

The x-ray generation procedure is initiated by tracking a large number of high-energy electrons continuously bombarding the target. As mentioned above, MCNP uses a continuous slowing down approximation energy loss model for electron transport. According to this model, it breaks the electrons' path into many steps and substeps. The length of each substep derives from the total stopping power of the electron in the absorbing material. MCNP's electron cross section data including energy loss rate, substep lengths, multiple scattering, and probability distributions for the production of secondary particles (fluorescent x rays, knock-on electrons, and bremsstrahlung photons) are all previously tabulated with a predefined energy grid. Like many other MC codes, MCNP uses "condensed history" Monte Carlo method for electron transport in which the global effects of electron collisions (energy loss and change in direction) are simulated at the end of each track segment or step.[38] The energy loss is sampled from the Landau distribution with theoretical and empirical modifications[40] by which bremsstrahlung and impact ionization K x rays are ultimately born into the target medium. The Goudsmit–Saunderson multiple scattering theory is used to sample the distribution of angular deflections, so that the direction of the electron can change at the end of each track segment.[38] The fact that all cross sections are predetermined and reside in electron libraries has numerous advantages. In particular, it makes the Goudsmit–Saunderson theory possible to use with ease. However, as a compromise, the primary and secondary particles remain un-

TABLE I. Summary of setup conditions and parameters used in this study (over 200 different combinations of the following parameters were evaluated).

Crack depth range (μm)	Anode angle range (deg)	Tube voltage range (kVp)
0	6	50
5	8	70
8	10	80
10	12	100
15	14	120
20		
30		
50		

correlated, which can lead to some calculation artifacts.[41] Electrons and their descendents are all tracked to where they are absorbed in or escape from the anode block. The escaping photons that might have gone through target self-filtration are further attenuated by the exit window and added filters and ultimately their transport is terminated in scoring regions specified at a distant point out of the x-ray tube.

In this study, a monoenergetic, unidirectional rectangular source was defined as the source of electrons with dimensions similar to those of a conventional x-ray tube's filament. With respect to the anode angle, the size of the focal spot was therefore about $1 \times 6-7$ mm^2. As listed in Table I, the spectra were simulated in a tungsten target x-ray tube operated at conventional voltages for different anode surface models and angles. It should be noted that since the depth range of cracks among our sample anodes was determined to be about between 5 and 50 μm, the coverage of this range with more samples was achieved by creating some depths artificially. In all setups, the emitted spectra were attenuated by a total inherent filtration of 2.5 mm Al and air between the exit window and the detector modeled as point detector tally (F5) appointed to detect photon flux at a distance of 100 cm away from the focal spot.

II.D. Validation

The validation MCNP's output involves comparing simulated and experimentally measured spectra in order to determine whether it faithfully reproduces realistic x-ray spectra. Due to the finite energy resolution of physical detectors, tungsten K-lines of all measured spectra appear as broadened peaks. Hence, for the same energy bin, characteristic K x rays measured by physical detectors always have a lower intensity than those obtained using MC simulations.[42] The shape of a broadened peak can be approximated by a Gaussian function centered at K-line's energy with a width characteristic of the resolution of the employed spectrometer.[43] Detector response was realistically modeled using Gaussian energy broadening (GEB) in which the tallied energies are broadened by sampling from the user-provided Gaussian energy distribution.[38] In our validation, the GEB card was used and its associated parameters experimentally adjusted to fit

the full width at half peak maximum (FWHM) of the spectrometer to which simulated spectra were compared.
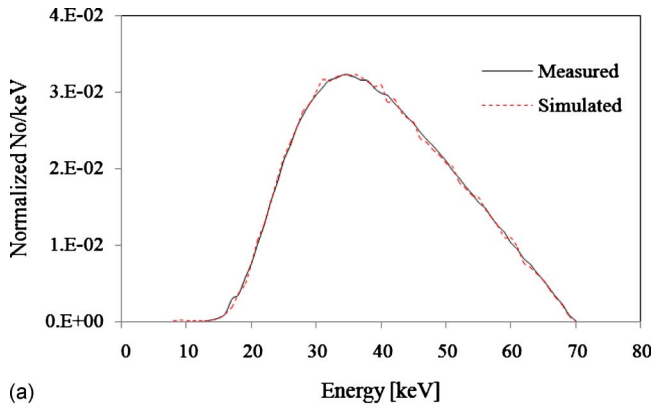
II.E. Quantitative assessment strategy

The simulated spectra of surface-cracked anodes were quantitatively assessed through comparison with simulated spectra in a perfectly plain anode under the same conditions of x-ray beam generation (anode angle, tube voltage, detection point, etc.). The figures of merit used for comparative assessment include the variations in shape and intensity of the spectra, HVL, anode heel effect, and patient dose. The filtering effect of anode roughness reduces both the quality and quantity of the outwardly emitted photons and as such intensity loss was used as a large in scope criterion. Also quantifying the overall variations in the spectra was completed using the normalized root mean squared difference (NRMSD), a well-established measure of the difference between estimates predicted by a model and the observed estimates normalized to the range of observed estimates. On the other hand, since diagnostic x-ray spectra are polychromatic, one can judge the penetrating ability of the emitted photons by calculating the HVL from transmission curves. The transmission curves were calculated by dividing transmitted air kerma through aluminum filter by air kerma in the absence of the filter. Attenuation coefficients data derived from the NIST XCOM photon cross section library[44] were used for filtering the spectra and calculating the air kerma. The heel effect, which refers to a falloff in the intensity of radiation field toward the anode side as a result of anode self-filtration,[29] was assessed by placing several point detectors along the anode-cathode direction and keeping them 100 cm away from the focal spot. Finally, change in patient skin entrance dose resulting from anode roughness in chest x-ray radiography examinations was assessed under various conditions using advanced computational models.[45]
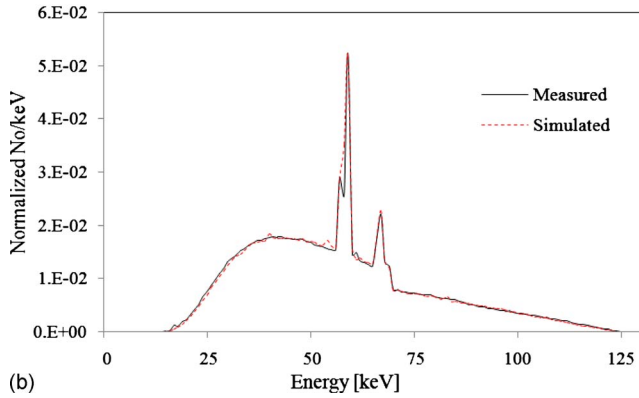
III. RESULTS

Figure 3 compares measured and simulated spectra for tube voltages of 70 and 125 kVp (anode angle 6°, total filtration 2.5 mm Al). The spectra measured using a highly pure germanium detector with a FWHM of 0.5 keV at 122 keV (^{57}Co) at the center of the radiation field was obtained from Ref. 46. Both spectra were binned into 1 keV energy intervals and normalized to the sum of all counts. In both simulations run using 8×10^7 electrons, the GEB card was invoked and provided with appropriate coefficients. As can be seen, the measured and simulated spectra are in very good agreement.

Figure 4 compares simulated spectra in a plain surface anode (used as reference) and those in rough anodes at tube voltages of 50, 70, 100, and 120 kVp and anode angle of 6°. As could be expected, depending on the depth of cracks (in Fig. 5: 10, 20, and 50 μm) both bremsstrahlung and characteristic K x rays were more attenuated as they experienced further inherent filtration particularly in the roughest anode models which were roughened by 50 μm deep cracks. The resulting filtration of emerging x rays also depends on the
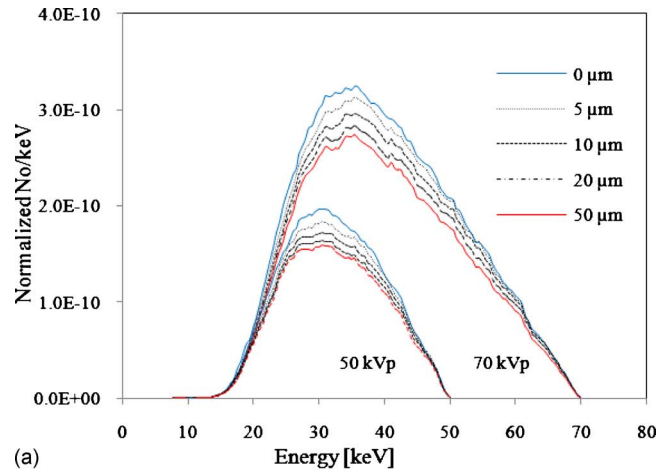
FIG. 3. Comparison of experimental and MCNP4C-simulated x-ray spectra at (a) 70 and (b) 125 kVp for a 6° tungsten anode with 2.5 mm Al filtration.
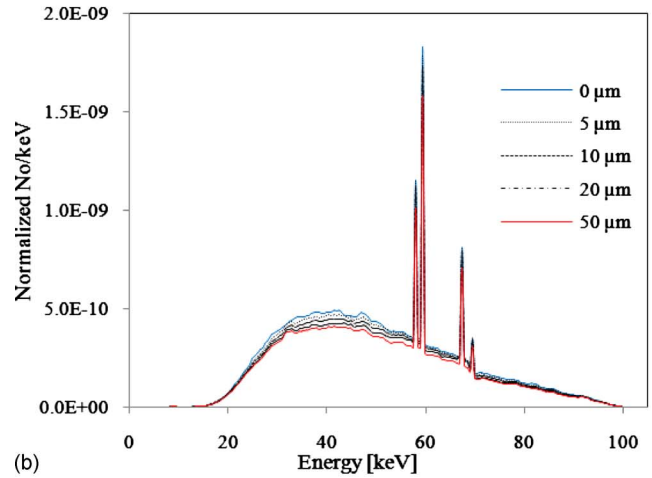
anode material, tube voltage, and anode angle.[31] In all investigated models, pure tungsten was used as anode's building material since in the process of electron impact ionization, which, like photoelectric absorption results in characteristic photons, MCNP's electron libraries only take into account K shell impact ionization in the highest Z component of the anode material.[38]

The dependence on tube voltage is fully appreciable especially at 50 kVp voltage. As tube voltage increases, the influence of anode roughness is limited to lower energy regions of the spectrum and hence the amount of photon absorption or intensity loss decreases. Table II presents the percentage of intensity loss for different crack depths, tube voltages and anode angles calculated by simulating 3.5×10^7 electrons. According to these results, the magnitude of intensity loss increases by decreasing tube voltage and anode angle and increasing the depth of cracks. For example, the intensity loss exceeds 16% at voltage of 50 kVp and anode angle of 6° for a crack depth of 50 μm.
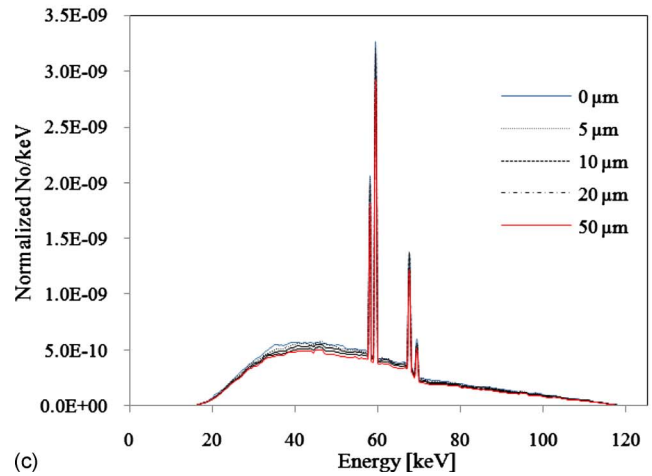
When quantified using NRMSD, the variations in spectral shape were found to be more pronounced for spectra generated at lower voltages in anodes having deeper cracks and smaller angles. Table III summarizes the percentage of NRMSD calculated for some of the generated spectra. The results seem to confirm once again that as cracks get deeper, tube voltage lower, and anode angle smaller, the output spectrum undergoes a heavier inherent filtration. By computing the first HVLs of these filtered spectra from transmission

FIG. 4. Comparison of simulated spectra of rough surface anodes with those of plain surface anodes for different crack depths at (a) 50 and 70, (b) 100, and (c) 120 kVp. (6° tungsten anode with 2.5 mm Al filtration).

curves and comparing them with the first HVLs of their reference spectra, it turned out that the effect of anode roughness on variations in HVL is far less notable than on intensity. The results are summarized in Table IV. The variations were exceedingly small; no spectrum was hardened by more
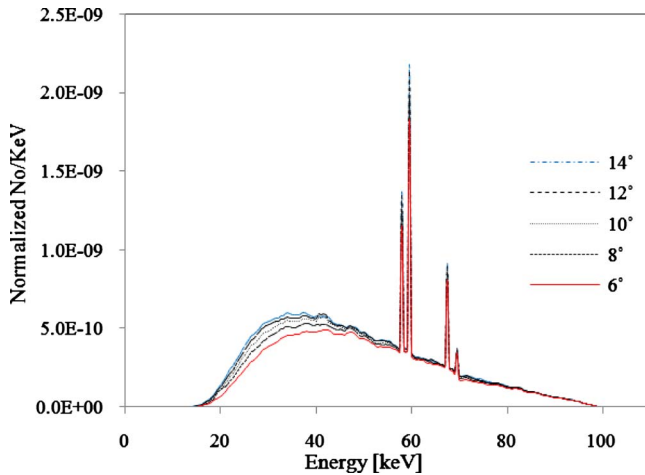
FIG. 5. Simulated x-ray spectra detected on the central axis for different target angles of plain tungsten anodes at 100 kVp tube voltage (2.5 mm Al filtration).

than 2.5%. When averaged over all the values, the variations in HVL ranged from $0.5 \pm 0.8\%$ to $1.4 \pm 0.9\%$ for 6° and 14° anodes, respectively.

For the assessment of anode heel effect and its variation with anode roughness, photon spectra were acquired using point detectors along anode-cathode axis for different target angles (6°–14°) and compared with each other. Figure 5 compares photon spectra generated in plain anodes detected at the central axis for the above mentioned target angles and

100 kVp voltage. These simulations show that when the target angle steeps from 14° to 6°, the output spectrum can lose up to 13% of its intensity and can get harder by increasing its HVL from 3.16 to 3.74 mm Al. Figure 6 shows the spectra of both plain and 50 μm deep cracked anodes for 6° and 14° target angles at 100 kVp. In the case of surface-cracked anodes, when the target angle decreases from 14° to 6°, intensity loss increases from about 5% to 18%, whereas the beam's HVL increases from 3.21 to 3.71 mm Al.

Figure 7 shows the variations in exposure (normalized per incident electrons) on anode-cathode axis for spectra generated in plain and rough surface anode with 6° and 12° target angles and 70 and 120 kVp tube voltages. As can be seen, anode roughness has caused an overall reduction in exposure throughout the radiation field. It was found that for an anode tilted by 6° and roughened by 50 μm deep cracks, the total exposure averaged over all detection points was reduced by 14.9% and 13.1% for 70 and 120 kVp tube voltages, respectively. Similarly, for an anode angle of 12°, the total exposure was reduced by 15.3% and 11.0%.

Figure 8 shows the variation in patient entrance skin dose (ESD) during chest x-ray radiography for an anode angle of 12° as a function of crack depth for various tube voltages (between 50 and 140 kVp). The results show that as anode roughness increases, patient entrance skin dose decreases averagely by a factor of 15%. As an example, for anodes roughened by 50 μm deep cracks, the ESD decreases by 16.5% and 13.8%, respectively.

TABLE II. Percentage of intensity loss for different crack depths, tube voltages, and anode angles. The spectra were filtered using 2.5 mm aluminum and detected at 100 cm from the focal spot.

Anode angle (deg)	Crack depth (μm)	Tube voltage (kVp)				
		50	70	80	100	120
6	5	4.5	3.0	3.1	2.9	2.1
	8	7.7	5.6	5.5	5.0	4.1
	10	9.3	7.1	7.0	6.3	5.3
	15	12.0	9.9	9.3	8.7	7.7
	20	13.6	11.6	11.3	10.4	9.5
	30	15.3	13.8	13.6	12.9	11.9
	50	16.8	15.9	15.7	15.3	14.1
10	5	2.1	1.5	1.4	1.3	1.2
	8	4.4	3.0	2.9	2.8	2.2
	10	5.9	4.0	3.8	3.5	3.0
	15	8.8	6.5	6.3	5.6	5.0
	20	11.0	8.6	8.2	7.4	6.7
	30	13.4	11.2	10.8	9.9	9.2
	50	15.7	14.0	13.6	13.1	12.3
14	5	1.1	1.0	0.7	0.7	0.6
	8	2.4	1.9	1.4	1.5	1.2
	10	3.6	2.5	2.1	2.0	1.6
	15	6.2	4.3	4.0	3.3	3.1
	20	8.7	5.9	5.5	4.7	4.4
	30	11.7	8.7	8.1	7.3	6.8
	50	14.4	11.8	11.4	10.2	9.8

TABLE III. Percentage of variation in the NRMSD for different crack depths, tube voltages, and anode angles.

Anode angle (deg)	Crack depth (μm)	Tube voltage (kVp)				
		50	70	80	100	120
6	5	3.4	2.3	1.6	0.6	0.4
	8	5.6	4.1	2.6	1.0	0.6
	10	6.6	5.1	3.3	1.2	0.7
	15	8.3	7.1	4.4	1.7	1.0
	20	9.7	8.1	5.2	2.0	1.2
	30	10.8	9.6	6.3	2.5	1.5
	50	12.0	10.9	7.4	3.0	1.8
10	5	1.8	1.5	1.1	0.4	0.3
	8	3.2	2.5	1.9	0.7	0.4
	10	4.1	3.2	2.3	0.8	0.5
	15	6.1	4.9	3.4	1.2	0.7
	20	7.6	6.3	4.2	1.5	0.9
	30	9.2	7.9	5.3	2.0	1.2
	50	10.7	9.9	6.7	2.6	1.6
14	5	1.3	1.2	0.8	0.3	0.2
	8	1.9	1.9	1.2	0.4	0.3
	10	2.7	2.3	1.5	0.5	0.3
	15	4.3	3.4	2.4	0.8	0.5
	20	5.9	4.7	3.2	1.0	0.6
	30	7.9	6.5	4.4	1.5	0.9
	50	9.7	8.6	5.8	2.0	1.2

IV. DISCUSSION

The prediction of the x-ray spectrum emitted from an x-ray tube can be accurately performed by Monte Carlo simulation. For this purpose, a number of general-purpose MC codes exit. In this work, we used the MCNP code owing to its powerful geometry package,[35] which allows simulating an x-ray spectrum in the complex geometry of deteriorated targets. The second motivation behind this choice is the experience gathered with this code which seems to provide more accurate predictions against other MC codes.[37] As shown in Fig. 3, the comparison with experimental spectra proved that under similar conditions, MCNP (through its GEB card) can faithfully predict the spectra. The minor mismatch observed in Fig. 3(b) in the region between tungsten $K\alpha_1$ and $K\alpha_2$ peaks where the MC results (using point detector tally) could not resolve peaks as good as the physical detector can be explained by the fact that the detector response is approximated by a Gaussian function whose coefficients may not be perfectly adjusted. However, the small value of NRMSD in both comparisons (1.2% for 70 kVp spectra and 1.8% for 125 kVp spectra) indicates a close agreement between the measured and simulated spectra. It is worth to note that by running 8×10^7 electrons and making use of point detector tally, a partially deterministic variance reduction technique,[38] the relative error of photon flux was minimized to 0.21%.

Previous MC studies reported that electrons with energies within radiologic voltages can penetrate into plain tungsten slabs between 2.5 and 14 μm.[46] When such electrons fall into the anode's cracks, particularly the parents, they can

deep more down. Hence, those useful x rays that were shallowly produced must go through a longer attenuating path before reaching the anode's surface. The direct result of this increased absorption, as seen in Fig. 4, is a loss of intensity in the detected spectra. Due to the inverse relationship between photon energy and attenuation coefficients, the increased filtration affects primarily low-to-medium energy photons especially at lower tube voltage. In addition, photons from the higher-energy portions of the spectrum are preferentially created near the anode surface,[31] and as such they take a shorter track toward the surface and consequently are less attenuated.

Figure 9 shows the trend in output variation against anode angle and tube voltage for the minimum and maximum crack depths studied in this work. The range of intensity loss for anodes having 5 and 50 μm deep cracks is 3.8% and 7.0%, respectively. This indicates that the spectra emitted from not-so-much aged tubes are less affected by variations in anode angle and tube voltage. As the steepness of anode angle increases, the attenuation of x rays, in particular low-energy ones, becomes more severe and as such the output intensity is reduced to a greater extent.

Our results are in good agreement with the work of Erdelyi et al.[34] where a 5% intensity loss for anode angle of 6° and tube voltage of 100 kVp was reported for an 8 μm mean depth of the cracks. The difference (1% increase) is likely due to the empirical approach followed by the authors as well as the assumption that electrons strike the anode surface at normal incidence and that the associated x rays do not scatter in the anode block. Although there is no *a priori*
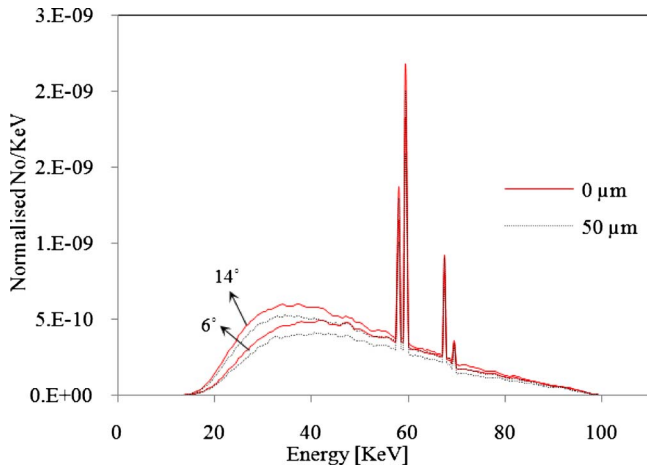
FIG. 6. Comparison of spectra produced in plain and 50 μm deep cracked anodes for 6° and 14° target angles at 100 kVp tube voltage (2.5 mm Al filtration).
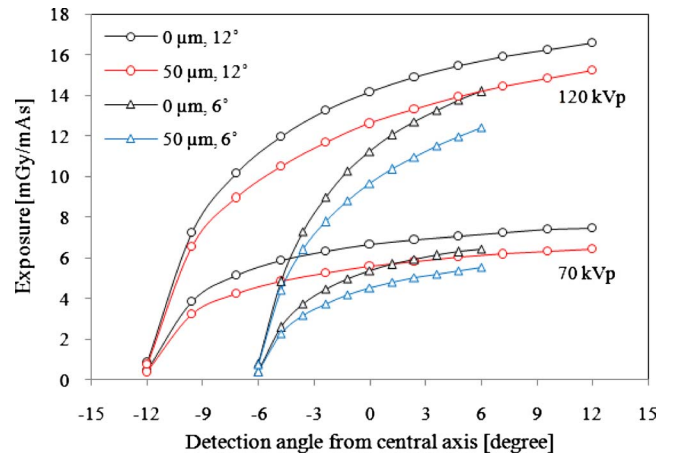

FIG. 7. Effect of anode roughness on overall reduction in exposure in anode-cathode axis. The spectra have been produced in plain and 50 μm deep cracked anodes with 6° and 12° angles and 70 and 120 kVp tube voltages.

known upper limit in the anode roughness, Lenz[30] claimed that long-term tests have demonstrated that anode roughness at the end of a typical tube's lifespan can reach 45 μm, which might cause a weakening of output radiation by 14% or even more. Consistent with this report, our results point to a loss of output intensity of 14.78% averaged over the studied voltages in a typical aged x-ray tube (mean crack depth of 50 μm, anode angle of 10°, and total filtration of 2.5 mm Al). However, our results showed that the variations in HVL with roughness are much less than those reported in the literature[31,32] but the overall trend is that the HVL increases

with crack depth. It was found that the largest variation in HVL occurs at around 70 kVp. In addition, at voltages lower than 70 kVp there are some negatively increased HVLs for deep cracks which implies that the increased anode self-filtering has attenuated not only low-to-medium but also high-energy photons which has resulted in beam softening [Fig. 4(a)]. In general, an increase of 0.03 mm Al and a decrease of 0.005 mm Al were obtained for the HVL of spectra produced in 5 and 50 μm deep cracked anodes at 70 kVp, respectively. Assuredly, this discrepancy must be ascribed to the way and accuracy of obtaining output air

TABLE IV. Percentage of HVL variation for different crack depths, tube voltages, and anode angles.

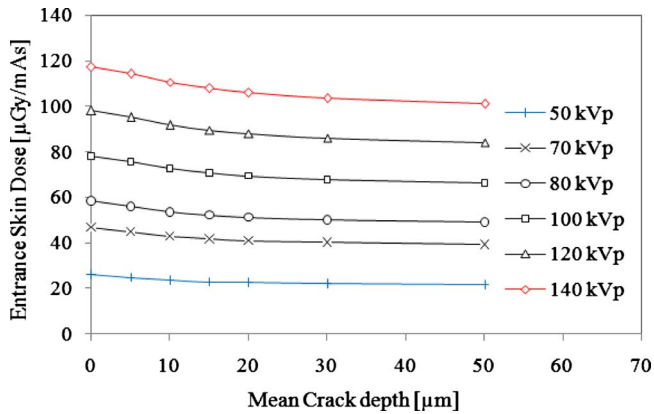| Anode angle (deg)	Crack depth (μm)	Tube voltage (kVp)				
		50	70	80	100	120
6	5	−0.1	1.1	1.4	0.4	1.3
	8	0.0	1.3	1.6	0.7	1.6
	10	−0.8	1.2	1.7	0.7	1.9
	15	−0.6	0.9	1.6	0.5	1.4
	20	−0.9	0.5	0.7	0.3	1.0
	30	−0.8	0.2	0.4	−0.2	0.6
	50	−0.8	−0.2	−0.2	−0.8	0.1
10	5	1.7	0.9	1.5	1.2	1.1
	8	1.3	1.4	1.8	1.8	1.5
	10	1.9	1.5	2.4	2.1	1.8
	15	1.9	1.7	2.4	2.5	2.1
	20	1.9	2.2	2.4	2.1	1.9
	30	1.4	1.0	1.9	1.9	1.9
	50	1.2	0.6	1.2	1.1	1.4
14	5	0.0	0.7	1.1	0.8	0.5
	8	0.2	1.2	1.6	1.5	1.3
	10	0.0	1.4	1.8	1.7	1.6
	15	0.2	1.8	2.4	2.2	2.1
	20	0.0	2.1	2.5	2.5	2.5
	30	−0.4	1.7	2.1	2.5	2.4
	50	−0.4	1.3	1.5	2.2	2.2

FIG. 8. Variation in patient ESD during x-ray chest radiography for rough surface anodes having 0–50 μm deep cracks, tube potentials varying between 50 and 140 kVp, and anode angle of 12°.

kerma. In experimental measurements, along with anode roughening there are other factors such as voltage ripple that contribute to the variations in output kerma. Hence, the value derived from the work of Nagel[31] may be subjected to some uncertainty. Nowotny and Meghzifene[32] employed the XCOMP5R code[47] which is based on Birch and Marshall model, while we used MCNP4C-based Monte Carlo transport of electrons by sampling their interactions from more accurate cross section data.[48] Most empirical and semiempirical models rely on unphysical parameters that describe the shape of bremsstrahlung distribution and its normalizations. Since five parameters are used by the Birch and Marshall model, applying them to new or unconventional x-ray tube designs may be accompanied by some miscalculations.[49] Furthermore, comparisons between measured and calculated air kerma using Birch and Marshall-based codes have demonstrated an overestimation of calculated kerma.[33,50] Ay *et al.*[37] reported on average overestimation of 9.5%–14.4% for kerma derived using XCOMP5R for tube voltages from 80 to 120 kV, 12.5° tungsten target and 1.2 mm Al inherent filtration, whereas MCNP4C resulted in estimates between 2.0 and 4.4%. By invoking MCNP's GEB card along with PHYS
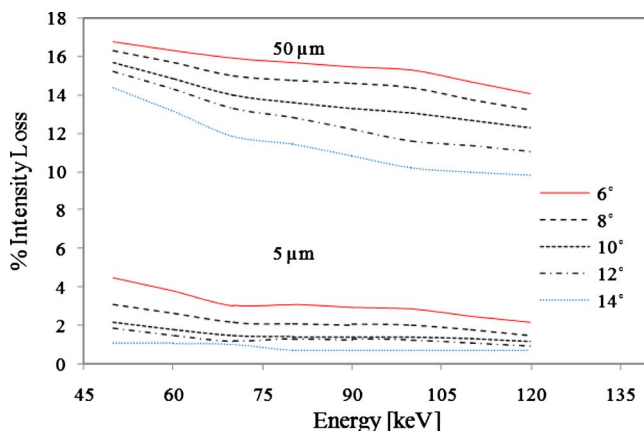
card, a useful card for biasing some physical parameters, the bias will certainly be further reduced.

Despite the capabilities of accurate MC modeling used in this work, it is worth to highlight some of the assumptions made for anode models. For the abovementioned reason, by ignoring the roughness of regions bounded by parent cracks, the added filtering effect of these regions was assumed to be negligible. This assumption should be reasonable for less deteriorated anodes in tubes operating at high voltages. Although cracks were modeled with a range of widths, it was assumed that all of them have the same depth equal to mean surface roughness (R_a). This assumption is fairly reasonable because the decreased filtration of those deep cracks that became shallow is compensated by the increased filtration of shallow cracks that are being deepened. Finally, it was assumed that all cracks are rectangular in their route, which allowed using simpler surfaces in geometry definition. The results presented here should be applicable for quality control of aged x-ray tubes and might find applications in many radiological investigations.

V. CONCLUSION

The current study attempted to pave the way for better understanding of the influence of anode surface roughness on diagnostic x-ray spectra, an influencing factor that has been addressed in a limited number of investigations. By employing the MCNP4C code, a Monte Carlo simulation was performed to redress the insufficiencies of previously used analytical models. By following an image-based modeling, it was attempted to define more realistic models for anode roughness. SEM measurements showed a significant grain growth and crack formation in our most aged anode and surface profilometry determined that its center line average roughness (R_a) can go up to 50 μm. An intensity loss of 16.8% was predicted for anodes aged by 50 μm deep cracks (50 kVp, target angle 6°, total filtration 2.5 mm Al). It was found that the first HVL of spectra is insignificantly affected by roughness but the overall trend is that the HVL increases with roughness. Simulated projection radiographies showed that at equal exposure conditions, an increase in anode roughness results in a decrease in patient entrance skin radiation dose. We conclude that depending on x-ray tube's workload, anode roughening should be considered with care in medical x-ray imaging systems.

ACKNOWLEDGMENTS

FIG. 9. Trends in output variation against anode angles and tube voltages for anodes having 5 and 50 μm deep cracks (2.5 mm Al filtration).

[a] Electronic mail: habib.zaidi@hcuge.ch

[1] E. L. Nickoloff and H. L. Berman, "Factors affecting x-ray spectra," Radiographics **13**, 1337–1348 (1993).

[2] M. Matsumoto, H. Kubota, H. Hayashi, and H. Kanamori, "Effects of voltage ripple and current mode on diagnostic x-ray spectra and exposures," Med. Phys. **18**, 921–927 (1991).

[3] A. G. Haus, C. E. Metz, J. T. Chiles, and K. Rossmann, "The effect of x ray spectra from molybdenum and tungsten target tubes on image quality in mammography," Radiology **118**, 705–709 (1976).

[4]L. Desponds, C. Depeursinge, M. Grecescu, C. Hessler, A. Samiri, and J. F. Valley, "Influence of anode and filter material on image quality and glandular dose for screen-film mammography," Phys. Med. Biol. **36**, 1165–1182 (1991).

[5]N. A. Gkanatsios, W. Huda, and K. Peters, "Effect of radiographic techniques (kVp and mAs) on image quality and patient doses in digital subtraction angiography," Med. Phys. **29**, 1643–1650 (2002).

[6]S. J. Glick, S. Thacker, X. Gong, and B. Liu, "Evaluating the impact of x-ray spectral shape on image quality in flat-panel CT breast imaging," Med. Phys. **34**, 5–24 (2007).

[7]K. A. Fetterly and N. J. Hangiandreou, "Effects of x-ray spectra on the DQE of a computed radiography system," Med. Phys. **28**, 241–249 (2001).

[8]W. Zhao, W. G. Ji, and J. A. Rowlands, "Effects of characteristic x rays on the noise power spectra and detective quantum efficiency of photoconductive x-ray detectors," Med. Phys. **28**, 2039–2049 (2001).

[9]S. J. Glick, S. Vedantham, and A. Karellas, "Investigation of optimal kVp setting for CT mammography using a flat-panel imager," Proc. SPIE **4682**, 392–402 (2002).

[10]J. T. Dobbins III, E. Samei, H. G. Chotas, R. J. Warp, A. H. Baydush, C. E. Floyd, Jr., and C. E. Ravin, "Chest radiography: Optimization of x-ray spectrum for cesium iodide-amorphous silicon flat-panel detector," Radiology **226**, 221–230 (2003).

[11]M. Yaffe, K. W. Taylor, and H. E. Johns, "Spectroscopy of diagnostic x rays by a Compton scatter method," Med. Phys. **3**, 328–334 (1976).

[12]M. S. Nogueira, H. C. Mota, and L. L. Campos, "(HP)Ge measurement of spectra for diagnostic x-ray beams," Radiat. Prot. Dosim. **111**, 105–110 (2004).

[13]K. Maeda, M. Matsumoto, and A. Taniguchi, "Compton-scattering measurement of diagnostic x-ray spectrum using high-resolution Schottky CdTe detector," Med. Phys. **32**, 1542–1547 (2005).

[14]M. R. Ay and H. Zaidi, "Analytical and Monte Carlo X-ray Spectra Modeling in Mammography" in *Emerging Technology in Breast Imaging and Mammography*, edited by J. Suri, R. M. Rangayyan, and S. Laxminarayan (American Scientific, Valencia, 2007), 25–44.

[15]B. R. Archer, T. R. Fewell, and L. K. Wagner, "Laplace reconstruction of experimental diagnostic x-ray spectra," Med. Phys. **15**, 832–837 (1988).

[16]P. H. Huang, T. S. Chen, and K. R. Kase, "Reconstruction of diagnostic x-ray spectra by numerical analysis of transmission data," Med. Phys. **13**, 707–710 (1986).

[17]J. M. Boone, T. R. Fewell, and R. J. Jennings, "Molybdenum, rhodium, and tungsten anode spectral models using interpolating polynomials with application to mammography," Med. Phys. **24**, 1863–1874 (1997).

[18]J. M. Boone and J. A. Seibert, "An accurate method for computer-generating tungsten anode x-ray spectra from 30 to 140 kV," Med. Phys. **24**, 1661–1670 (1997).

[19]H. A. Kramers, "On the theory of x-ray absorption and of the continuous x-ray spectrum," Philos. Mag. **46**, 836–871 (1923).

[20]W. J. Iles, "The computation of the bremsstrahlung x-ray spectra over an energy range 15 keV to 300 keV," National Radiological Protection Board Report No. NRPB-R204, 1987.

[21]B. W. Soole, "A method of x-ray attenuation analysis for approximating the intensity distribution at its point of origin of bremsstrahlung excited in a thick target by incident electrons of constant medium energy," Phys. Med. Biol. **21**, 369–389 (1976).

[22]R. Birch and M. Marshall, "Computation of bremsstrahlung x-ray spectra and comparison with spectra measured with a Ge(Li) detector," Phys. Med. Biol. **24**, 505–517 (1979).

[23]D. M. Tucker, G. T. Barnes, and D. P. Chakraborty, "Semiempirical model for generating tungsten target x-ray spectra," Med. Phys. **18**, 211–218 (1991).

[24]D. M. Tucker, G. T. Barnes, and X. Z. Wu, "Molybdenum target x-ray spectra: A semiempirical model," Med. Phys. **18**, 402–407 (1991).

[25]X. Llovet, L. Sorbier, C. S. Campos, E. Acosta, and F. Salvat, "Monte Carlo simulation of x-ray spectra generated by kilo-electron-volt electrons," J. Appl. Phys. **93**, 3844–3851 (2003).

[26]H. Zaidi, "Relevance of accurate Monte Carlo modeling in nuclear medical imaging," Med. Phys. **26**, 574–608 (1999).

[27]K. E. Sale, Livermore National Laboratory, Report No. UCRL-JC-132644 (1999).

[28]W. R. Hendee and E. R. Ritenour, *Medical Imaging Physics*, 4th ed. (Wiley-Liss, Inc., New York, 2002).

[29]J. T. Bushberg, J. A. Setbert, E. M. Letdholdt, and J. M. Boon, *The Essential Physics of Medical Imaging*, 2nd ed. (Lippincott Williams & Wilkins, Philadelphia, 2002).

[30]E. Lenz, X-ray anode having an electron incident surface scored by microslits, Siemens Aktiengesellschaft, Munich (2006).

[31]H. D. Nagel, "Limitations in the determination of total filtration of x-ray tube assemblies," Phys. Med. Biol. **33**, 271–289 (1988).

[32]R. Nowotny and K. Meghzifene, "Simulation of the effect of anode surface roughness on diagnostic x-ray spectra," Phys. Med. Biol. **47**, 3973–3983 (2002).

[33]K. Meghzifene, H. Aiginger, and R. Nowotny, "A fit method for the determination of inherent filtration with diagnostic x-ray units," Phys. Med. Biol. **51**, 2585–2597 (2006).

[34]M. Erdélyi, M. Lajko, R. Kakonyi, and G. Szabo, "Measurement of the x-ray tube anodes' surface profile and its effects on the x-ray spectra," Med. Phys. **36**, 587–593 (2009).

[35]D. W. Rogers, "Fifty years of Monte Carlo simulations for medical physics," Phys. Med. Biol. **51**, R287–R301 (2006).

[36]M. R. Ay, M. Shahriari, S. Sarkar, M. Adib, and H. Zaidi, "Monte Carlo simulation of x-ray spectra in diagnostic radiology and mammography using MCNP4C," Phys. Med. Biol. **49**, 4897–4917 (2004).

[37]M. R. Ay, S. Sarkar, M. Shahriari, D. Sardari, and H. Zaidi, "Assessment of different computational models for generation of x-ray spectra in diagnostic radiology and mammography," Med. Phys. **32**, 1660–1675 (2005).

[38]J. F. Briesmeister, "MCNP—A general Monte Carlo N-particle transport code," Los Alamos National Laboratory Report No. LA-13709-M, 2000.

[39]Y. Wu, "CAD-based interface programs for fusion neutron transport simulation," Fusion Eng. Des. **84**, 1987–1992 (2009).

[40]O. Chibani and X. A. Li, "Monte Carlo dose calculations in homogeneous media and at interfaces: A comparison between GEPTS, EGSnrc, MCNP, and measurements," Med. Phys. **29**, 835–847 (2002).

[41]S. M. Seltzer, "Electron-photon Monte Carlo calculations: The ETRAN code," Appl. Radiat. Isot. **42**, 917–941 (1991).

[42]M. Bazalova and F. Verhaegen, "Monte Carlo simulation of a computed tomography x-ray tube," Phys. Med. Biol. **52**, 5945–5955 (2007).

[43]W. A. Metwally, R. P. Gardner, and A. Snood, "Gaussian broadening of MCNP pulse height spectra," Trans. Am. Nucl. Soc. **91**, 789–790 (2004).

[44]J. H. Hubbell and S. M. Seltzer, Tables of X-ray mass attenuation coefficients and mass energy-absorption coefficients, NISTIR 5632. National Institute of Standards and Technology, Gaithersburg (1987).

[45]G. Zubal, C. Harrell, E. Smith, Z. Ratner, G. Gindi, and P. Hoffer, "Computerized three-dimensional segmented human anatomy," Med. Phys. **21**, 299–302 (1994).

[46]G. G. Poludniowski and P. M. Evans, "Calculation of x-ray spectra emerging from an x-ray tube. Part I. electron penetration characteristics in x-ray targets," Med. Phys. **34**, 2164–2174 (2007).

[47]R. Nowotny and A. Hvfer, "Ein Programm fur die Berechnung von diagnostischen Roentgenspektren," Fortschr Roentgenstr **142**, 685–689 (1985).

[48]J. R. Mercier, D. T. Kopp, W. D. McDavid, S. B. Dove, J. L. Lancaster, and D. M. Tucker, "Modification and benchmarking of MCNP for low-energy tungsten spectra," Med. Phys. **27**, 2680–2687 (2000).

[49]G. G. Poludniowski, "Calculation of x-ray spectra emerging from an x-ray tube. Part II. X-ray production and filtration in x-ray targets," Med. Phys. **34**, 2175–2186 (2007).

[50]P. Meyer, E. Buffard, L. Mertz, C. Kennel, A. Constantinesco, and P. Siffert, "Evaluation of the use of six diagnostic x-ray spectra computer codes," Br. J. Radiol. **77**, 224–230 (2004).